This article has been accepted for publication in a future issue of this journal, but has not been fully edited. Content may change prior to final publication. Citation information: DOI 10.1109/TNS.2017.2717864, IEEE Transactions on Nuclear Science

Euler's Elastica Strategy for Limited-angle Computed Tomography Image Reconstruction

Hanming Zhang, Linyuan Wang, Yuping Duan, Lei Li, Guoen Hu, Bin Yan*

***Abstract*—Limited-angle computed tomography (CT) image reconstruction is a noteworthy reconstruction problem in which image prior models are crucial. In this work, we aimed to develop an appropriate regularization-based method to suppress the aliasing artifacts and improve the image quality for limited-angle CT image reconstruction. Given the observation that the isophotes of reconstructed images in specific missing directions, which are not tangent to the available projection rays, are usually broken and have large curvatures, a curvature-driven Euler's elastica regularization is introduced to rectify large curvatures and keep the isophotes smooth without erratic distortions. The developed approach is evaluated using numerical simulation and real CT data, and is compared with TV, and TGV-based reconstructions. Both qualitative and quantitative evaluation results demonstrate that a prospective performance can be obtained using the proposed Euler's elastica-based method for limited-angle tomography. This method has excellent aliasing artifact suppression and edge preservation.**

***Index Terms*—Computed tomography, limited angle problem, Euler's elastica, image reconstruction.**

I. Introduction

Limited-angle tomography is a common problem in many applications, such as digital dental radiography [1], digital breast tomosynthesis[2], and industrial inspection [3]. Image reconstruction from limited-angle projections can be treated as an inverse problem that is inherently ill-posed and difficult to converge to the correct solution without additional prior information, which is because of the available angular range of the sinogram being less than the ideal 180 °. Therefore, target image reconstruction from a limited-angle scan is challenging in medical imaging.

In the past decades, various methods have been proposed to recover the details and decrease the artifacts for limited-angle computed tomography (CT) image reconstruction. Two strategies have been widely investigated: 1) improving reconstruction algorithms, such as iterative reconstruction re-projection [4], projection onto convex sets [5], and sinogram extrapolation [6-8], and 2) using additional prior knowledge. Recently, using additional prior information has been intensively studied for limited-angle problems. Prior knowledge can be divided into two categories: one is to directly reflect the specific information of object structure and the other one is to indicate the object properties. Preoperative prior information, such as surfaces and similar prior images [9-11], is useful for improving image quality, but it is usually difficult to obtain and sometimes even unavailable. Conversely, prior information indicating object properties is relatively easy to gain. Therefore, it is often introduced as additional regularization terms into iterative reconstruction.

Following compressive sensing theory [12], prior knowledge involving sparse properties has recently gained attention for CT image reconstruction. Total variation (TV) regularization using image gradient sparsity is popular and widely used for incomplete data reconstruction issues [13-17]. To improve the performance of TV and eliminate staircase effect, higher-order derivatives[18], such as total variation stokes(TVS) model [19], and total generalized variation (TGV) model [20-22], have been studied. Moreover, wavelet and curvelet-based [7, 23] sparse models have also been studied. These regularization methods involving sparse prior information have shown obvious improvements in artifact suppression for data loss caused by metal implants [24], angular undersampling, and data truncation [15, 18, 25]. In limited-angle scanning, these methods can recover the missing information gradually when data inconsistency is limited to a certain range. However, real CT data acquisitions often contain various noises, scattering, and beam hardening, it is difficult to obtain a reliable solution and the reconstructed image usually suffers from aliasing artifacts.

Investigating specific characterizations of limited-angle scanning is another potential way to achieve satisfactory images. The scanning angular coverage is directionally incomplete; therefore, reconstructions usually have directional features in which details are not in tangent to the projection rays and difficult to be recovered [26-27]. On the basis of this observation, Chen et al. [28] argued the unsuitability of the standard TV model to solve the limited-angle problem and proposed an improved anisotropic model. Thus, a suitable prior model relative to the specific scanning characteristics is important to obtaining satisfactory reconstructions for limited-angle tomography.

Most regularization-based methods only consider a property

This work is supported in part by the National Natural Science Foundation of China under Grants No. 61372172 and 61601518. (Corresponding author: Bin Yan.)

H. Zhang, L. Wang, L. Li, G. Hu and B. Yan are with National Digital Switching System Engineering and Technological Research Center, Zhengzhou, 450002, P.R.China. (E-mail: z.hanming@hotmail.com; wanglinyuanwly@163.com; leehotline@aliyun.com; guoenhu@126.com; ybspace@hotmail.com).

Y. Duan is with Center for Applied Mathematics, Tianjin University, Tianjin, 300072, P.R.China. (E-mail: yuping.duan@tju.edu.cn).

0018-9499 (c) 2016 IEEE. Personal use is permitted, but republication/redistribution requires IEEE permission. See http://www.ieee.org/publications_standards/publications/rights/index.html for more information.

This article has been accepted for publication in a future issue of this journal, but has not been fully edited. Content may change prior to final publication. Citation information: DOI 10.1109/TNS.2017.2717864, IEEE Transactions on Nuclear Science

description of the whole image and are commonly incapable of tackling missing directional problems. Therefore, severe blurs usually arise in the missing directions of the reconstructed images. We examined the visual connectivity of the objects and found that the isophotes in these regions were easy to be multiplexed and broken; the isophote curvatures were significantly larger than those of the original ones. Therefore, a solution using continuous and smooth isophotes seemed suitable for limited-angle image reconstruction. To preserve the isophotes, a Euler's elastica model [29] which utilizes both TV and curvature minimization has been studied for image inpainting. The numerical solutions of Euler's elastica functional is complex and time consuming. In 2011, Tai et al. [30] applied the augmented Lagrangian method to Euler's elastica model and proposed a fast and efficient (Tai-Hahn-Chung-11, THC-11) algorithm. Euler's elastica-based methods show good performance in detail preservation from imperfectly sampled data for many image processing applications [30-31].

Inspired by Tai et al.'s work, this paper aims at developing a curvature-driven strategy to solve the limited-angle problem and extending the THC-11 algorithm for specific CT image reconstruction task. The Euler's elastica-based CT image reconstruction model is introduced and an alternating direction minimization-based optimization method is developed. The developed Euler's elastica-based method could compensate for the broken gaps and recover details with continuous, smooth isophotes. Thus, this method performs effectively in aliasing reduction and detail recovery for limited-angle CT image reconstruction.

The rest of this paper is organized as follows: In Section 2, the curvature-driven strategy for limited-angle problem is introduced. In Section 3, the proposed Euler's elastic-based reconstruction framework and its optimization scheme are described. Then, the experimental designs and quantitative studies on simulated and real data are reported in Sections 4 and 5, respectively. Finally, related issues are discussed.

II. Curvature-driven Strategy for the Limited-angle Problem

A. TV Regularization Model

The TV regularization method exploits the sparsity of the gradient magnitude image. Mathematically, the original TV of an image $\mathbf{u}:\Omega\to\mathbb{R}$ is defined as

$$E(\mathbf{u})=\int_{\Omega}|\nabla\mathbf{u}|dx, \tag{1}$$

where Ω is a bound domain, and ∇ represents a discrete gradient operator.

To solve for a minimizer of TV function, the steepest descent method can be used according to the following equation:

$$0=\nabla\cdot\frac{\nabla\mathbf{u}}{|\nabla\mathbf{u}|}. \tag{2}$$

Therefore, the solver of the TV model can be interpreted as diffusion, with diffusivity equal to $1/|\nabla\mathbf{u}|$, which depends on the gradient magnitude.

However, in the limited-angle scans, the deficiency in continuous angular data hinders detail recovery in the radical directions that are parallel to the projection rays [26]. In this case, a gradient-driven diffusion cannot guarantee a certain minimum and may result in copies and blurs in the region along the missing radical directions. Figure 1 shows a reconstruction of a uniform-density torus using the SART-TV method. The available angular coverage of a fan-beam CT scanning is 90°. The result indicates the gaps and blocky blurs in the originally smooth and continuous edges caused by the gradient-driven diffusion.

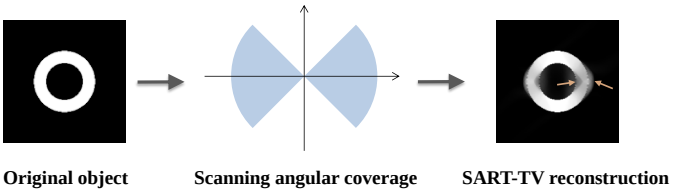

Fig. 1. SART-TV reconstructions on a uniform-density torus with limited-angle projections.

B. Curvature-based Euler's Elastica Regularization Model

To most human eyes, the preferred reconstruction in Figure 1 is to connect the broken gaps and recover the torus with continuous sharp boundaries. A favorable solution is to have clearer level sets. To mediate the TV model shortage, a suitable solution is to consider the isophotes. In Figure 2, the isophotes in TV-based reconstruction are broken with patches and blurs, whereas those in the original image are smooth. Blurs and patches cause large curvatures. Therefore, a suitable way to mediate the limited-angle problem is to prevent the large curvatures in isophotes.

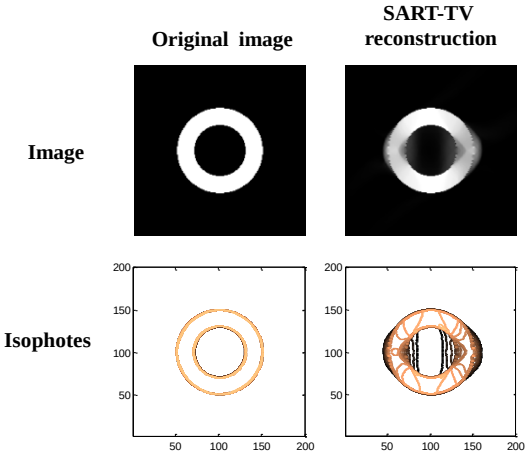

Fig. 2. Isophotes of a TV-based reconstruction image in a limited-angle scan.

To satisfy the visual connectivity principle and penalize large curvatures, a curvature-driven diffusion is introduced. Following Ref. [29], a new diffusion strength $|\kappa|^p/|\nabla\mathbf{u}|$ is used instead of $1/|\nabla\mathbf{u}|$, where $\kappa=\nabla\cdot\frac{\nabla\mathbf{u}}{|\nabla\mathbf{u}|}$ denotes the curvature of isophotes of $\mathbf{u}$ and $p>0$. The introduction of the curvature-driven strategy strengthens the diffusion process when the curvature of an isophote is large and weakens it when

0018-9499 (c) 2016 IEEE. Personal use is permitted, but republication/redistribution requires IEEE permission. See http://www.ieee.org/publications_standards/publications/rights/index.html for more information.

This article has been accepted for publication in a future issue of this journal, but has not been fully edited. Content may change prior to final publication. Citation information: DOI 10.1109/TNS.2017.2717864, IEEE Transactions on Nuclear Science

the curvature is small. Thus, the curvature-driven model smoothens the isophotes, causes the boundaries to be more continuous, and restrains the blocky blurs.

The TV-based model seeks a solution with the smallest variation in intensity, whereas the curvature-based model seeks a solution with the smoothest isophotes. The gradient- and curvature-driven diffusions represent two different philosophies. To combine the advantages of the two methods, a combination model called Euler's elastica [29–31] is adopted for limited-angle problems. The Euler's elastica energy is defined as follows:

$$E(\mathbf{u}) = \int_{\Omega} \left(a + b\kappa^2\right) |\nabla \mathbf{u}| dx. \tag{3}$$

where a corresponds to minimizing the TV of image, and b corresponds to minimizing the isophote curvature. The two terms are balanced through the weights a and b. They can lead to desirable and smooth isophotes without noticeable broken gaps and avoid excessive smoothness that may cover details. Therefore, Euler's elastica regularization model-based method can promote performance for limited-angle CT image reconstruction.

III. CT Image Reconstruction using Euler's Elastica Regularization

A. Imaging Model and Objective Function

The CT imaging model can be approximated using the discrete linear system:

$$\mathbf{p} = \mathbf{A}\mathbf{u}, \tag{4}$$

where vector $\mathbf{p}$ represents the projection data, vector $\mathbf{u}$ is the object to be reconstructed, and $\mathbf{A}$ is the projection matrix.

To solve the CT image reconstruction problem using Euler's elastica regularization method, we propose to minimize the following function:

$$\min_{\mathbf{u}} \sum_{i,j} \left(a + b \left(\nabla \frac{\nabla \mathbf{u}(i.j)}{|\nabla \mathbf{u}(i.j)|} \right)^2 \right) |\nabla \mathbf{u}(i.j)| \qquad s.t. \quad \|\mathbf{A}\mathbf{u} - \mathbf{p}\|_2 \le \varepsilon. \tag{5}$$

where ε is a tolerance parameter that sets an upper boundary in the allowable discrepancy between estimated and available data, and i and j are the index of pixels and $i \in [1, N_1]$, $j \in [1, N_2]$, respectively.

B. Optimization Approach

To derive the solution for the minimization problem in (5), we apply the alternating direction minimization (ADM) method based on the augmented Lagrangian method [30, 33–34] to obtain efficient and easy-to-code algorithms. By introducing the vectors $\mathbf{s}$, $\mathbf{n}$, and $\mathbf{m}$, we consider the following constrained minimization problem, which is equivalent to (5):

$$\min_{\mathbf{u},\mathbf{s},\mathbf{n},\mathbf{m}} \sum_{i,j} \left(\left(a + b\left(\nabla \mathbf{n}(i.j)\right)^2 \right) |\mathbf{s}(i.j)| \right), \quad s.t. \begin{cases} \mathbf{A}\mathbf{u} - \mathbf{p} = \mathbf{e}, \quad \|\mathbf{e}\|_2 \le \varepsilon, \\ \mathbf{s} = \nabla \mathbf{u}, \\ \mathbf{n} = \mathbf{m}, \\ |\mathbf{s}| = \mathbf{m} \cdot \mathbf{s}, \\ |\mathbf{m}| \le 1. \end{cases} \tag{6}$$

The minimization problem (5) can be converted to derive the saddle-point of the augmented Lagrangian energy. The augmented Lagrangian energy $\mathcal{L}_A$ associated with (6) can be expressed as

$$\begin{aligned} \mathcal{L}_A = & \sum_{i,j} \left(\left(a + b\left(\nabla \mathbf{n}(i.j)\right)^2 \right) |\mathbf{s}(i.j)| \right) + \frac{\mu}{2} \|\mathbf{A}\mathbf{u} - \mathbf{p} - \mathbf{e}\|_2^2 \\ & + \mathbf{r}_1^{\mathrm{T}} \left(|\mathbf{s}| - \mathbf{m} \cdot \mathbf{s} \right) + \lambda_1 \sum_i \left(|\mathbf{s}_i| - \mathbf{m}_i \cdot \mathbf{s}_i \right) \\ & + \mathbf{r}_2^{\mathrm{T}} \left(\mathbf{s} - \nabla \mathbf{u} \right) + \frac{\lambda_2}{2} \|\mathbf{s} - \nabla \mathbf{u}\|_2^2 \\ & + \mathbf{r}_3^{\mathrm{T}} \left(\mathbf{n} - \mathbf{m} \right) + \frac{\lambda_3}{2} \|\mathbf{n} - \mathbf{m}\|_2^2 + \delta_R(\mathbf{m}), \end{aligned} \tag{7}$$

where $\mathbf{r_1}$, $\mathbf{r_2}$, and $\mathbf{r_3}$ are Lagrange multipliers, λ_1, λ_2, λ_3, and μ are positive constants used to balance the terms, and the function $\delta_R(\cdot)$ is defined as follows:

$$\delta_R(\mathbf{m}) = \begin{cases} 0, & \mathbf{m} \in \mathbb{R}, \\ +\infty, & \text{otherwise.} \end{cases} \tag{8}$$

To obtain accurate results, the half-point differencing method [30–31] was used in numerical implementation. As shown in Figure 3, for one point on •-nodes, the first and second components of the relative differences are defined on its neighborhood ○- and □-nodes, respectively.

Some notations are introduced first according to the above grid definition. Without loss of generality, we represent a grayscale image to be reconstructed as an $N_1 \times N_2$ matrix. The Euclidean space $R^{N_1 \times N_2}$ is denoted as V. The discrete backward and forward differential operators are defined using periodic boundary condition as follows:

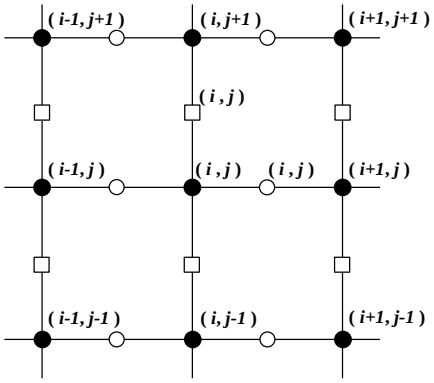

Fig. 3. Grid definition. The rule of indexing variables in the augmented Lagrangian function (7): $\mathbf{u}$ and $\mathbf{r}_1$ are defined on •-nodes. The first and second components of $\mathbf{s}$, $\mathbf{n}$, $\mathbf{m}$, $\mathbf{r}_2$, and $\mathbf{r}_3$ are defined on ○-nodes and □-nodes, respectively..

0018-9499 (c) 2016 IEEE. Personal use is permitted, but republication/redistribution requires IEEE permission. See http://www.ieee.org/publications_standards/publications/rights/index.html for more information.

This article has been accepted for publication in a future issue of this journal, but has not been fully edited. Content may change prior to final publication. Citation information: DOI 10.1109/TNS.2017.2717864, IEEE Transactions on Nuclear Science

$$\partial_1^- \mathbf{u}(i,j) = \begin{cases} \mathbf{u}(i,j) - \mathbf{u}(i-1,j), & 1<i \le N_1, \\ \mathbf{u}(1,j) - \mathbf{u}(N_1,j), & i = 1, \end{cases} \tag{9}$$

$$\partial_2^- \mathbf{u}(i,j) = \begin{cases} \mathbf{u}(i,j) - \mathbf{u}(i,j-1), & 1< j \le N_2, \\ \mathbf{u}(i,1) - \mathbf{u}(i,N_2), & j = 1, \end{cases} \tag{10}$$

$$\partial_1^+ \mathbf{u}(i,j) = \begin{cases} \mathbf{u}(i+1,j) - \mathbf{u}(i,j), & 1 \le i < N_1, \\ \mathbf{u}(1,j) - \mathbf{u}(N_1,j), & i = N_1, \end{cases} \tag{11}$$

$$\partial_2^+ \mathbf{u}(i,j) = \begin{cases} \mathbf{u}(i,j+1) - \mathbf{u}(i,j), & 1 \le j < N_2, \\ \mathbf{u}(i,1) - \mathbf{u}(i,N_2), & j = N_2. \end{cases} \tag{12}$$

The discrete gradient operator $\nabla : V \to Q$, where $Q = V \times V$, and the discrete divergence operator $\mathrm{div} : Q \to V$ are defined for $u \in V$, and $s \in Q$, respectively

$$\nabla \mathbf{u}(i,j) := \left(\partial_1^+ \mathbf{u}(i,j), \partial_2^+ \mathbf{u}(i,j) \right), \tag{13}$$

$$\mathrm{div}\mathbf{s}(i,j) := \partial_1^- \mathbf{s}_1(i,j) + \partial_2^- \mathbf{s}_2(i,j). \tag{14}$$

A special operator is defined to measure the magnitude of $\mathbf{s}$ at $(i,j) \in \bullet$-nodes, where $\mathbf{s}_1$ and $\mathbf{s}_2$ are defined on $\circ$-nodes and $\square$-nodes, respectively. The operator can be formulated as follows:

$$\mathcal{M}_{i,j}^{\bullet}(\mathbf{s}) = \left(\left(\frac{\mathbf{s}_1(i,j) + \mathbf{s}_1(i-1,j)}{2} \right)^2 + \left(\frac{\mathbf{s}_2(i,j) + \mathbf{s}_2(i,j-1)}{2} \right)^2 \right)^{\frac{1}{2}}. \tag{15}$$

The divergence of $\mathbf{n}$ at $(i,j) \in \bullet$-nodes can be computed as

$$\mathrm{div}_{i,j}^{\bullet}(\mathbf{n}) = \mathbf{n}_1(i,j) - \mathbf{n}_1(i-1,j) + \mathbf{n}_2(i,j) - \mathbf{n}_2(i,j-1). \tag{16}$$

Next, we explain how to solve the optimization problem (7) via ADM. The augmented Lagrangian function can be split into four subproblems with respect to $\mathbf{u}$, $\mathbf{s}$, $\mathbf{n}$, and $\mathbf{m}$, and the solution to minimizing $\mathcal{L}_A$ is equivalent to solving the subproblems alternately.

1) u-subproblem

The minimization problem with respect to $\mathbf{u}$ can be expressed as follows:

$$\mathbf{u}^{k+1} = \arg\min_{\mathbf{u}} \frac{\mu}{2} \left\| \mathbf{A}\mathbf{u} - \mathbf{p} - \mathbf{e}^k \right\|_2^2 + \frac{\lambda_2}{2} \left\| \mathbf{s}^k + \frac{\mathbf{r}_2^k}{\lambda_2} - \nabla \mathbf{u} \right\|_2^2. \tag{17}$$

Problem (17) can be solved using the linearization approximate method [35] to avoid pseudo-inverse computing. Let $\mathcal{F}$ stand for discrete Fourier transform. Therefore, we have

$$\mathbf{u}^{k+1} = \Re\left(\mathcal{F}^{-1}\left(\mathcal{F}\left(\frac{\mu}{\tau}\mathbf{u}^k - \mu \mathbf{A}^{\mathrm{T}}\left(\mathbf{A}\mathbf{u}^k - \mathbf{p} - \mathbf{e}^k \right) - \lambda_2 \mathrm{div}\left(\mathbf{s}^k + \frac{\mathbf{r}_2^k}{\lambda_2} \right) \right) \Big/ \mathbf{G} \right) \right), \tag{18}$$

where $\mathbf{G} = \mathrm{diag}\left[\mathcal{F}\left(\frac{\mu}{\tau}\mathbf{I} - \lambda_2 \mathrm{div}\nabla \right) \mathcal{F}^{-1} \right]$, and $\tau > 0$ is a parameter. In this work, τ is typically set to 1.0.

The noise term is updated as follows:

$$\mathbf{e}^{k+1} = \min\left\{ 1,\ \varepsilon \Big/ \left\| \mathbf{A}\mathbf{u}^{k+1} - \mathbf{p} \right\|_2 \right\} \cdot \left(\mathbf{A}\mathbf{u}^{k+1} - \mathbf{p} \right), \tag{19}$$

2) s-subproblem

The optimization problem for variable $\mathbf{s}$ can be reformulated as

$$\mathbf{s}^{k+1} = \arg\min_{\mathbf{s}} \sum_{i,j} \left(\left(a + b\left(\nabla \mathbf{n}^k(i.j) \right)^2 + \lambda_1 + \mathbf{r}_1^k(i.j) \right) \left| \mathbf{s}(i.j) \right| \right) + \frac{\lambda_2}{2} \left\| \mathbf{s} - \nabla \mathbf{u}^{k+1} - \frac{\lambda_1 + \mathbf{r}_1^k}{\lambda_2} \mathbf{m}^k + \frac{\mathbf{r}_2^k}{\lambda_2} \right\|_2^2. \tag{20}$$

This problem can be solved using the shrinkage method [30, 33]. The minimizer $\mathbf{s}$ is derived by

$$\mathbf{s}^{k+1}(i.j) = \max\left\{ 1 - \frac{\mathbf{c}^k}{\lambda_2 \left| \mathbf{q}^k(i.j) \right|}, 0 \right\} \mathbf{q}^k(i.j), \tag{21}$$

where $\mathbf{c}^k = a + b\left(\nabla \mathbf{n}^k \right)^2 + \lambda_1 + \mathbf{r}_1^k$, and $\mathbf{q}^k = \nabla \mathbf{u}^{k+1} + \frac{\lambda_1 + \mathbf{r}_1^k}{\lambda_2} \mathbf{m}^k - \frac{\mathbf{r}_2^k}{\lambda_2}$.

3) n-subproblem

The minimization problem related to $\mathbf{n}$ can be expressed as

$$\mathbf{n}^{k+1} = \arg\min_{\mathbf{n}} \sum_{i,j} \left(b\left(\nabla \mathbf{n}(i.j) \right)^2 \left| \mathbf{s}^{k+1}(i.j) \right| \right) + \frac{\lambda_3}{2} \left\| \frac{\mathbf{r}_3^k}{\lambda_3} + \mathbf{n} - \mathbf{m}^k \right\|_2^2. \tag{22}$$

Similar to [30], the frozen coefficient method is applied to solve this problem. Thus, we obtain the following:

$$\mathbf{n}_1^{k+1} = \Re\left(\mathcal{F}^{-1}\left(\frac{t_{22}\mathcal{F}(\mathbf{f}_1) - t_{12}\mathcal{F}(\mathbf{f}_2)}{D} \right) \right), \tag{23}$$

$$\mathbf{n}_2^{k+1} = \Re\left(\mathcal{F}^{-1}\left(\frac{-t_{21}\mathcal{F}(\mathbf{f}_1) + t_{11}\mathcal{F}(\mathbf{f}_2)}{D} \right) \right), \tag{24}$$

where

$$\mathbf{f}_1(i,j) = \lambda_3 \mathbf{m}_1^k(i,j) - \mathbf{r}_{31}^k(i,j) - \left(g - 2b\mathcal{M}_{i+1,j}^{\bullet}\left(\mathbf{s}^{k+1} \right) \right) \mathrm{div}_{i+1,j}^{\bullet}\left(\mathbf{n}^k \right) + \left(g - 2b\mathcal{M}_{i,j}^{\bullet}\left(\mathbf{s}^{k+1} \right) \right) \mathrm{div}_{i,j}^{\bullet}\left(\mathbf{n}^k \right), \tag{25}$$

$$\mathbf{f}_2(i,j) = \lambda_3 \mathbf{m}_2^k(i,j) - \mathbf{r}_{32}^k(i,j) - \left(g - 2b\mathcal{M}_{i,j+1}^{\bullet}\left(\mathbf{s}^{k+1} \right) \right) \mathrm{div}_{i,j+1}^{\bullet}\left(\mathbf{n}^k \right) + \left(g - 2b\mathcal{M}_{i,j}^{\bullet}\left(\mathbf{s}^{k+1} \right) \right) \mathrm{div}_{i,j}^{\bullet}\left(\mathbf{n}^k \right), \tag{26}$$

and

$$t_{11} = \lambda_3 - 2g\left(\cos z_i - 1 \right), \tag{27}$$

$$t_{12} = g\left(1 - \cos z_j + \sqrt{-1}\sin z_i \right)\left(1 - \cos z_i - \sqrt{-1}\sin z_j \right), \tag{28}$$

$$t_{21} = g\left(1 - \cos z_i + \sqrt{-1}\sin z_j \right)\left(1 - \cos z_j - \sqrt{-1}\sin z_i \right), \tag{29}$$

$$t_{22} = \lambda_3 - 2g\left(\cos z_j - 1 \right), \tag{30}$$

$$D = \lambda_3^2 - 4g\lambda_3\left(\cos z_i + \cos z_j - 2 \right). \tag{31}$$

Here, $z_i = \frac{2\pi}{N_1}\omega_i, \quad \omega_i = 1, \ldots, N_1$ and $z_j = \frac{2\pi}{N_2}\omega_j, \quad \omega_j = 1, \ldots, N_2$, where y_i and y_i are the discrete frequencies in the frequency domain. Moreover, $g = \max_{i,j}\left(2b\mathcal{M}_{i,j}^{\bullet}\left(\mathbf{s}^{k+1} \right) \right)$.

0018-9499 (c) 2016 IEEE. Personal use is permitted, but republication/redistribution requires IEEE permission. See http://www.ieee.org/publications_standards/publications/rights/index.html for more information.

This article has been accepted for publication in a future issue of this journal, but has not been fully edited. Content may change prior to final publication. Citation information: DOI 10.1109/TNS.2017.2717864, IEEE Transactions on Nuclear Science

4) m-subproblem

The minimization problem with respect to $\mathbf{m}$ can be expressed as follows:

$$\mathbf{m}^{k+1} = \arg\min_{\mathbf{m}} \frac{\lambda_3}{2} \left\| \frac{\left(\mathbf{r}_1^k + \lambda_1\right)\mathbf{s}^{k+1} + \mathbf{r}_3^k}{\lambda_3} + \mathbf{n}^{k+1} - \mathbf{m} \right\|_2^2 + \delta_R(\mathbf{m}). \tag{32}$$

The associative projection [36] of this problem can be computed as follows:

$$\begin{aligned} \mathbf{m}^{k+1} &= \mathrm{proj}_{\mathcal{R}}(\mathbf{v}), \\ &= \begin{cases} \mathbf{v} & |\mathbf{v}| \le 1, \\ \mathbf{v}/|\mathbf{v}| & \text{otherwise}, \end{cases} \end{aligned} \tag{33}$$

where $\mathbf{v} = \dfrac{\left(\mathbf{r}_1^k + \lambda_1\right)\mathbf{s}^{k+1} + \mathbf{r}_3^k}{\lambda_3} + \mathbf{n}^{k+1}$.

5) Updating the Lagrange multipliers

Finally, the Lagrange multipliers are updated as follows:

$$\mathbf{r}_1^{k+1} = \mathbf{r}_1^k + \lambda_1\left(\left|\mathbf{s}^{k+1}\right| - \mathbf{m}^{k+1} \cdot \mathbf{s}^{k+1}\right) \quad \text{at } \bullet\text{-nodes}, \tag{34}$$

$$\mathbf{r}_{21}^{k+1} = \mathbf{r}_{21}^k + \lambda_2(\mathbf{s}_1^{k+1} - \partial_1^+ \mathbf{u}^{k+1}) \quad \text{at } \circ\text{-nodes}, \tag{35}$$

$$\mathbf{r}_{22}^{k+1} = \mathbf{r}_{22}^k + \lambda_2(\mathbf{s}_2^{k+1} - \partial_2^+ \mathbf{u}^{k+1}) \quad \text{at } \square\text{-nodes}, \tag{36}$$

$$\mathbf{r}_{31}^{k+1} = \mathbf{r}_{31}^k + \lambda_3(\mathbf{n}_1^{k+1} - \mathbf{m}_1^{k+1}) \quad \text{at } \circ\text{-nodes}, \tag{37}$$

$$\mathbf{r}_{32}^{k+1} = \mathbf{r}_{32}^k + \lambda_3(\mathbf{n}_2^{k+1} - \mathbf{m}_2^{k+1}) \quad \text{at } \square\text{-nodes}. \tag{38}$$

The augmented Lagrangian function (7) is expected to be minimized by solving the four subproblems alternately. All of the subproblems have noticeably efficient closed-form solutions: the *u*-subproblem and the *n*-subproblem are converted to the Fourier-based formulations, which can be calculated directly using FFT techniques; the *s*-subproblem is solved by shrinkage operator and the *m*-subproblem is solved by projector operator rapidly. Thus, the proposed algorithm is efficient and practical for the low cost in each iteration.

Algorithm 1: EE-ADM algorithm

Input $\mathbf{A}, \mathbf{p}, a, b, \lambda_1, \lambda_2, \lambda_3, \mu, \tau, \varepsilon$, initialize $\mathbf{u}^0, \mathbf{s}^0, \mathbf{n}^0, \mathbf{m}^0$, and $k = 0$.

While "not converged," **Do**

(1) updating $\mathbf{u}$ using equation (18);

(2) updating $\mathbf{e}$ using equation (19);

(3) updating $\mathbf{s}$ using equation (21);

(4) updating $\mathbf{n}$ using equations (23) and (24);

(5) updating $\mathbf{m}$ using equation (33);

(6) updating Lagrange multipliers $\mathbf{r}_1, \mathbf{r}_2$, and $\mathbf{r}_3$ using equations (34) to (38);

(7) $k \leftarrow k + 1$.

End Do

Obtain reconstruction result: $\mathbf{u}$.

The present method is called the Euler's elastica-based alternating direction minimization (EE-ADM). The overall workflow of the present EE-ADM method for X-ray CT image reconstruction is listed in Algorithm 1. The iteration can be stopped upon reaching the predefined criteria (e.g., the number of iterations and representation error).

C. Parameter Selections

The positive weights a and b are used to balance the TV and curvature terms of Euler's elastica model. Their proper values should be chosen on the basis of scanning configurations and specific features of the underlying image. Generally, $b > a$ is adequate for most applications. Moreover, $b/a \in [5, 20]$ may be suitable for the limited-angle CT image reconstruction task.

Parameters μ, λ_1, λ_2, and λ_3 are used to balance the data fidelity and regularization terms. For an optimal performance, their values should be set in accordance with both the noise level in the observation and the sparsity level of the underlying image. Moreover, they are empirically selected through visual inspection. Based on our experience, the higher the noise level is, the smaller the μ should be. $\lambda_1 \in [0.1, 10]$, $\lambda_2 \in [1, 1000]$ and $\lambda_3 \in [1, 500]$ provide suitable smoothing strength for most reconstruction objects.

IV. Experimental Design

A. Experimental Data Acquisition

To validate and evaluate the performance of the proposed EE-ADM algorithm in limited-angle CT image reconstruction, a computer-simulated digital Popeye phantom[37], and experimental anthropomorphic phantom datasets were used for the experiments.

(a) **(b)** **(c)**

Fig. 4. Digital and physical phantoms used in the studies: (a) a digital jaw phantom, (b) an anthropomorphic head phantom (Chengdu Dosimetric Phantom, CPET Co. Ltd, Chengdu, China), and (c) a slice of the anthropomorphic head phantom reconstructed using the SART-TV method with full 360 projections.

1) Digital Popeye phantom study

In the simulation study, a slice of a digital Popeye phantom designed by Pack et al. [37] was used. As shown in Figure 4(a), the Popeye phantom was modeled using anatomical abdominal structures and large arms. For the CT projection simulation, we chose a geometry representative of a fan-beam CT scanner setup. The imaging configurations were as follows: (1) the projection data of 360 projections at an interval of 1° onto a 1024-bin linear detector array, (2) 1000 cm distance from the detector to the X-ray source, (3) 500 cm distance from the

0018-9499 (c) 2016 IEEE. Personal use is permitted, but republication/redistribution requires IEEE permission. See http://www.ieee.org/publications_standards/publications/rights/index.html for more information.

This article has been accepted for publication in a future issue of this journal, but has not been fully edited. Content may change prior to final publication. Citation information: DOI 10.1109/TNS.2017.2717864, IEEE Transactions on Nuclear Science

rotation center to the source, and (4) 0.707 mm spacing between each detector bin. Each of the reconstructed images comprised 512 × 512 pixels. The size of each pixel was 0.5 mm × 0.5 mm. Each projection datum along the X-ray through the sectional image was calculated as the intersection length of an X-ray with a pixel. We extracted continuous 120- and 90-view projections from the sinogram data for illustration purposes.

In the simulation, noise was simulated and generated using a Poisson model as follows:

$$N_i = \text{Poisson}(N_0 \exp(-p_i)), \tag{39}$$

where N_0 is the incident X-ray intensity, and p_i denotes the normalized projection in real space. In the simulation, the noise level N_0 was set to 5×10^5.

2) Anthropomorphic head phantom study

To further demonstrate the capability of the EE-ADM method for a realistic CT system, we performed a radiological anthropomorphic head phantom (Chengdu Dosimetric Phantom, CPET Co. Ltd., Chengdu, China) study for clinical use. The phantom is shown in Figure 4(b), and its specifications are described in the ICRU Report 48 [38]. In this study, CT projection data were acquired using a CT scanner comprising an X-ray source (Hawkeye130, Thales, France) and a flat-panel detector (Varian 4030E, USA) at 120 kV and 200 μA. The duration of each X-ray pulse in each projection view was 180 ms during acquisition. The central slice of the sinogram data was extracted for 2D investigation and modeled with 1432 bins on a 1D detector for 2D image reconstruction. The associated imaging parameters of the CT scanner were as follows: (1) 360 projection views were acquired evenly for a 360 °rotation on an orbit, (2) the distance of the detector from the X-ray source was 998.75 mm, (3) the distance of the rotation center from the source was 529.16 mm, and (4) the space in between each detector bin was 0.296 mm. All of the reconstructed images comprised 512 × 512 pixels. The size of each pixel was 0.439 mm × 0.439 mm. For reference, a reconstructed reference slice from full 360 projections is presented in Figure 4(c). Two different cases of 120 ° available angular ranges were used to validate the performance of the proposed method.

B. Comparison Methods

To evaluate the performance of the present EE-ADM method, the TV-ADM[32] and TGV-ADM[21] methods were adopted for comparison. The optimization principle for TV-based method can be described as follows:

$$\min_{\mathbf{u}} \|\nabla \mathbf{u}\|_1 \quad s.t. \ \|\mathbf{A}\mathbf{u} - \mathbf{p}\|_2 \le \varepsilon. \tag{40}$$

And the constrained TGV minimization model for CT image reconstruction can be described as follows:

$$\min_{\mathbf{u},\boldsymbol{\omega}} \alpha_1 \|\nabla \mathbf{u} - \boldsymbol{\omega}\|_1 + \alpha_2 \|\kappa(\boldsymbol{\omega})\|_1, \quad s.t. \ \|\mathbf{A}\mathbf{u} - \mathbf{p}\|_2 \le \varepsilon \tag{41}$$

where $\kappa(\boldsymbol{\omega}) = \frac{1}{2}\left(\nabla \boldsymbol{\omega} + \nabla \boldsymbol{\omega}^{\mathrm{T}}\right)$ is a symmetrized gradient operator.

The augmented Lagrangian method was applied to solve the generated constrained TV and TGV minimization models. And for purposes of comparison, the proximal point technique [33] was also applied to avoid the prohibitive cost of pseudo-inverse computing for the **u**-subproblem.

In the experiments, the regularization parameters λ and μ of TV-ADM algorithm were set to 32, 64 for simulation and 16, 32 for real data study, respectively. For TGV-ADM method, α_1 and α_2 were set to 2 and 0.5, respectively. The regularization parameters λ_1, λ_2, and μ were set to 32, 32, 64 for simulation and 16, 16, 32 for real data study, respectively. The tolerance ε was set to 10^{-5}. The number of iterations was set to 1000 for simulation and 400 for real data study. The related parameters of the EE-ADM algorithm in the three groups of experiments are listed in Table I.

TABLE I
ALGORITHM PARAMETERS FOR THE SIMULATION AND REAL DATA STUDY.

		a	b	λ_1	λ_2	λ_3	μ
EE-ADM	Simulation	1	10	2	200	10	64
	Real data study	1	20	1	200	20	32

C. Performance Evaluation

To quantify the image quality, the root mean square error (RMSE), peak signal-to-noise ratio (PSNR), and universal quality index (UQI) [39] were used as deviation measures between the reconstructed images **f** and reference image $\mathbf{f}_{Ref}$.

RMSE and PSNR are used to measure the difference between two images. They are defined as follows:

$$RMSE = \sqrt{\frac{\sum_{i=1}^{N} |\mathbf{f}(i) - \mathbf{f}_{Ref}(i)|^2}{N}}, \tag{42}$$

$$PSNR = 10\log_{10}\left(\frac{MAX^2(\mathbf{f}_{Ref})}{\frac{1}{N}\sum_{i=1}^{N}|\mathbf{f}_{Ref}(i) - \mathbf{f}(i)|^2}\right) \text{ dB}, \tag{43}$$

where *N* is the total number of pixels in the image.

The mean, variance, and covariance of intensities are defined as follows:

$$\bar{\mathbf{f}}_{Ref} = \frac{1}{N}\sum_{i=1}^{N}\mathbf{f}_{Ref}(i), \ \sigma_{Ref}^2 = \frac{1}{N-1}\sum_{i=1}^{N}\left(\mathbf{f}_{Ref}(i) - \bar{\mathbf{f}}_{Ref}\right)^2, \tag{44}$$

$$\bar{\mathbf{f}} = \frac{1}{N}\sum_{i=1}^{N}\mathbf{f}(i), \ \sigma^2 = \frac{1}{N-1}\sum_{i=1}^{N}\left(\mathbf{f}(i) - \bar{\mathbf{f}}\right)^2, \tag{45}$$

$$Cov\left(\mathbf{f}_{Ref}, \mathbf{f}\right) = \frac{1}{N-1}\sum_{i=1}^{N}\left(\mathbf{f}_{Ref}(i) - \bar{\mathbf{f}}_{Ref}\right)\left(\mathbf{f}(i) - \bar{\mathbf{f}}\right), \tag{46}$$

Then, UQI can be calculated as follows:

$$UQI = \frac{2Cov\left(\mathbf{f}_{Ref}, \mathbf{f}\right)}{\sigma_{Ref}^2 + \sigma^2}\frac{2\bar{\mathbf{f}}_{Ref}\bar{\mathbf{f}}}{\bar{\mathbf{f}}_{Ref}^2 + \bar{\mathbf{f}}^2}. \tag{47}$$

A UQI value close to 1 indicates a high degree of similarity between the reconstructed and reference images.

0018-9499 (c) 2016 IEEE. Personal use is permitted, but republication/redistribution requires IEEE permission. See http://www.ieee.org/publications_standards/publications/rights/index.html for more information.

This article has been accepted for publication in a future issue of this journal, but has not been fully edited. Content may change prior to final publication. Citation information: DOI 10.1109/TNS.2017.2717864, IEEE Transactions on Nuclear Science

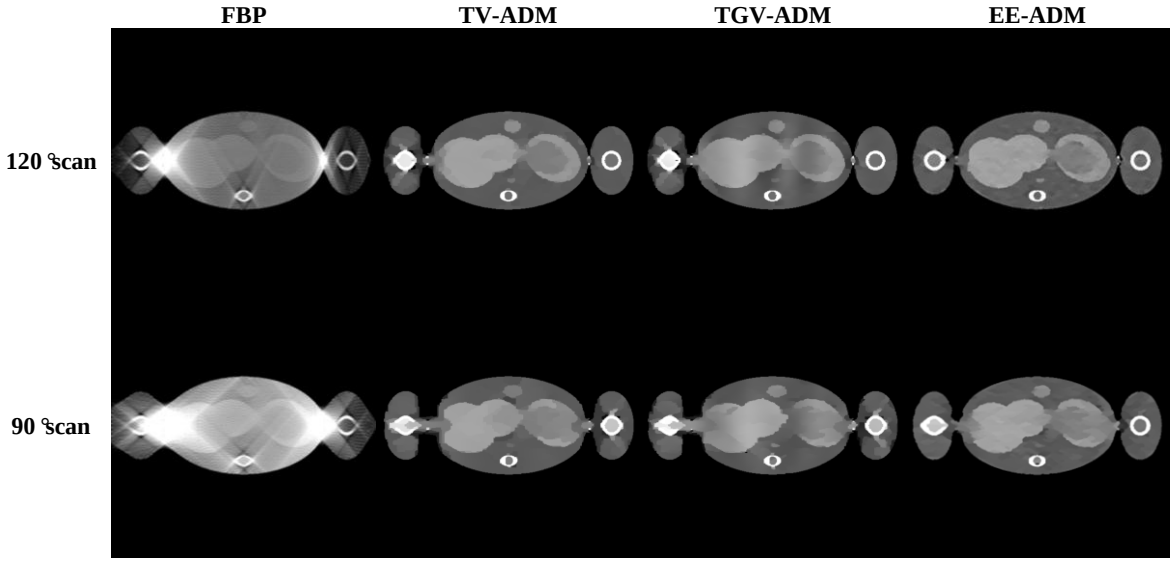

Fig. 5. Image reconstruction of the digital Popeye phantom. From left to right in each row, images reconstructed from FBP (C = 300 HU/W = 1000 HU), TV-ADM, TGV-ADM, and EE-ADM methods (C = 30 HU/W = 220 HU) are presented.

V. Results

A. Simulation Study

1) Visualization-based evaluation

Figure 5 shows the results reconstructed using FBP, TV-ADM, TGV-ADM, and EE-ADM methods with 120 °and 90 ° angular coverages. The images reconstructed using FBP exhibited severe distortions and artifacts, and the image quality could be improved using three iterative reconstruction methods. Recovering the information near the arms was difficult because of the missing continuous angular sinogram. In the TV-ADM and TGV-ADM reconstructions, the bone structures of arms were distorted. Compared with the TV and TGV-based results, the information in these regions obtained using EE-ADM method could be recovered more accurately. In addition to the reconstructions, the difference from the ground truth is displayed in Figure 6. The results showed that EE-ADM algorithm generated smaller errors than other counterparts.

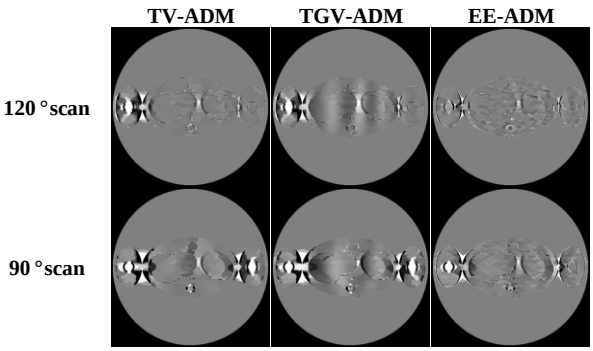

Fig. 6. Different images related to the ground truth of TV-ADM, TGV-ADM and EE-ADM reconstructions in the digital Popeye phantom study (C = 0 HU/W = 100 HU).

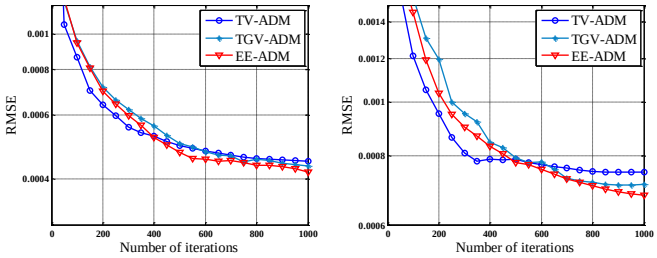

(a) 120 °scan **(b) 90 °scan**

Fig. 7. Root mean square errors as a function of iteration steps for the three iterative methods in the digital Popeye phantom study.

TABLE II
EVALUATIONS OF THE RESULTS RECONSTRUCTED USING DIFFERENT ALGORITHMS IN THE DIGITAL POPEYE PHANTOM STUDY.

		TV-ADM	TGV-ADM	EE-ADM
120 °	RMSE	4.472e-04	4.373e-04	4.172e-04
	PSNR	35.90 dB	36.28dB	36.64 dB
	UQI	0.9984	0.9985	0.9986
90 °	RMSE	7.466e-04	7.129e-04	6.692e-04
	PSNR	31.64 dB	31.97dB	32.46 dB
	UQI	0.9959	0.9961	0.9966

2) Convergence analysis

To test the convergence of the proposed method, the RMSE values of the reconstructions at the different iteration numbers were calculated; the calculation results are displayed in Figure 7 using a logarithmic scale. The results illustrated that EE-ADM algorithm could converge to a steady status for both scanning cases. Moreover, the convergence speed was increased as the available angular range increased with the fixed parameter settings.

0018-9499 (c) 2016 IEEE. Personal use is permitted, but republication/redistribution requires IEEE permission. See http://www.ieee.org/publications_standards/publications/rights/index.html for more information.

This article has been accepted for publication in a future issue of this journal, but has not been fully edited. Content may change prior to final publication. Citation information: DOI 10.1109/TNS.2017.2717864, IEEE Transactions on Nuclear Science

3) Quantitative evaluation

To quantify the performance of the proposed method, the RMSE, PSNR, and UQI of the reconstructions from the three iterative methods were calculated; the calculation results are listed in Table II. The quantitative results from the proposed EE-ADM method showed better results than those from other algorithms in terms of the three measurements.

4) Parameter Comparisons and Analyses

In this section we discuss the impacts of different parameters of EE-ADM algorithm on the reconstructed image quality for limited-angle CT image reconstruction. The balance between the TV and curvature terms is often adjusted by the positive weights a and b. Thus, we first focus the investigation on comparing the results reconstructed with different weights a and b.

The images reconstructed with different weights with 90° angular coverage are shown in Figure 8. And the relative PSNR measures of the reconstructed images are shown in Figure 9. The bone structure of left arm is difficult to recover and the TV-based reconstruction has blurred artifacts because of the loss of scanning projections. In Euler's elastica-based results, a large value of a/b may lead to a similar blurring and the reconstructed image with parameters (a = 10, b = 1) have indistinct artifacts. As the value of b increases, the broken gaps in the isophotes decrease as well, and the reconstructed image obtains improved visual connectivity. Thus, the structures in the specific region that have missing data could be recovered effectively. The structure of left arm of the reconstructed result with parameters (a = 1, b = 200) is recovered better than that of other results. However, a large selection of b may also lead to a decrease in image quality and result in an over-smooth effect that may overlook detailed textures. The adequate selection of the weights can be seen as a search for a balance between connectivity and smoothness information, and may be sensitive to data conditions.

Parameters λ_1, λ_2, and λ_3 are associated with Lagrange multipliers and play important roles in the algorithm. In 90° angular scanning case, the PSNR measures of the reconstructed images with different λ_1, λ_2, and λ_3 are displayed in Figure 10. All experiments were implemented with same parameters settings except the target parameter. All three penalty parameters have adequate selction ranges. The parameter λ_1 controls the closeness between $|\mathbf{s}|$ and $\mathbf{m}\cdot\mathbf{s}$, and it is set to 1 or 2 in most image reconstruction tasks for optimal performance and simple tuning. The parameter λ_2 controls the diffusion of $\mathbf{u}$. A proper initial value of λ_2 could be set to 100, and then be tuned based on specific tasks. The parameter λ_3 controls the closeness between $\mathbf{n}$ and $\mathbf{m}$. Based on our experience, a large λ_3 would lead a slow convergence speed. When the parameter λ_3 is too large, it may lead a unsuitable over-smooth result.

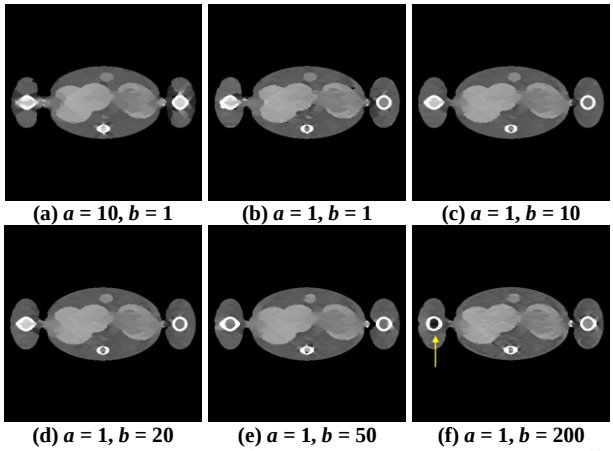

Fig. 8. Image reconstruction of the digital Popeye phantom with different weights (C = 30 HU/W = 220 HU).

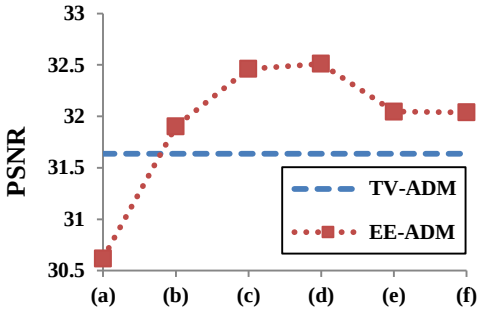

Fig. 9. PSNR measures of the results reconstructed with different groups of weights a and b. (a) a = 10, b = 1. (b) a = 1, b = 1. (c) a = 1, b = 10. (d) a = 1, b = 20. (e) a = 1, b = 50. (f) a = 1, b = 200..

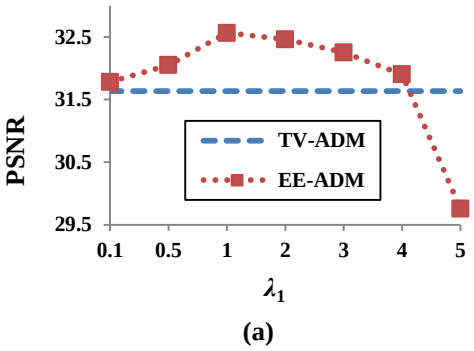

(a)

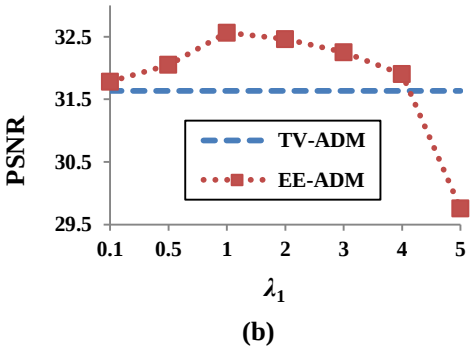

(b)

0018-9499 (c) 2016 IEEE. Personal use is permitted, but republication/redistribution requires IEEE permission. See http://www.ieee.org/publications_standards/publications/rights/index.html for more information.

This article has been accepted for publication in a future issue of this journal, but has not been fully edited. Content may change prior to final publication. Citation information: DOI 10.1109/TNS.2017.2717864, IEEE Transactions on Nuclear Science

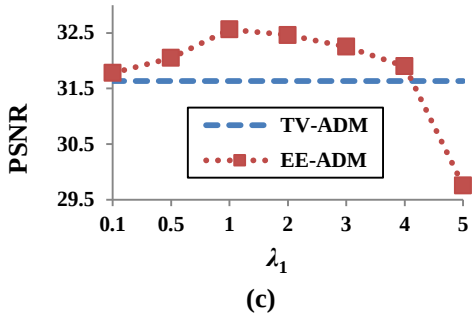

Fig. 10. Analysis on the EE-ADM reconstruction with respect to different values of λ_1, λ_2, and λ_3.

B. Real Data Study

1) Visualization-based evaluation

The reconstructed images of the anthropomorphic head phantom using different methods are presented in Figure 11. To reveal texture details, the zoomed region of interest (ROI) images of Case 1 and Case 2 are shown in Figure 12 and 13, respectively. Visual inspection of the results indicates that the TV-ADM and TGV-ADM result remains blurry and covers reliable information, whereas the EE-ADM method has an enhanced edge and detail preservation. In the TV-ADM reconstructed image, blurring and blocky artifacts were visible. TGV-ADM method suppressed the blocky artifacts but also suffered blurring distortions. EE-ADM method exhibits remarkable advantages over the other methods in terms of detail preservation.

2) Convergence analysis

Figure 14 shows the plot of the RMSE values versus the iteration steps for the TV-ADM, TGV-ADM and EE-ADM methods with a logarithmic scale for RMSE. The plots show that the present EE-ADM method can minimize the objective functions with a steady solution and that it exhibits improved accuracy when the reconstructed images are shrunk.

3) Quantitative evaluation

The RMSE, PSNR, and UQI of the reconstructed images in the anthropomorphic head phantom study are given in Table III. Results show that our method exhibits a prospective performance in terms of accuracy and resolution, consistent with the findings in Tables II.

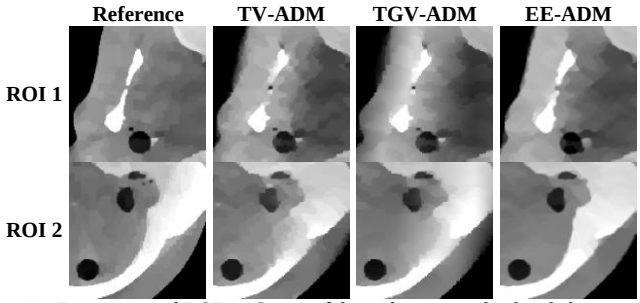

Fig. 12. Reconstructed ROIs in Case 1 of the anthropomorphic head phantom (C = 100 HU/W = 1500 HU).

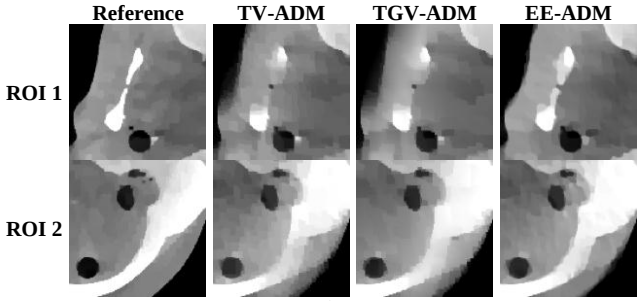

Fig. 13. Reconstructed ROIs in Case 2 of the anthropomorphic head phantom (C = 100 HU/W = 1500 HU).

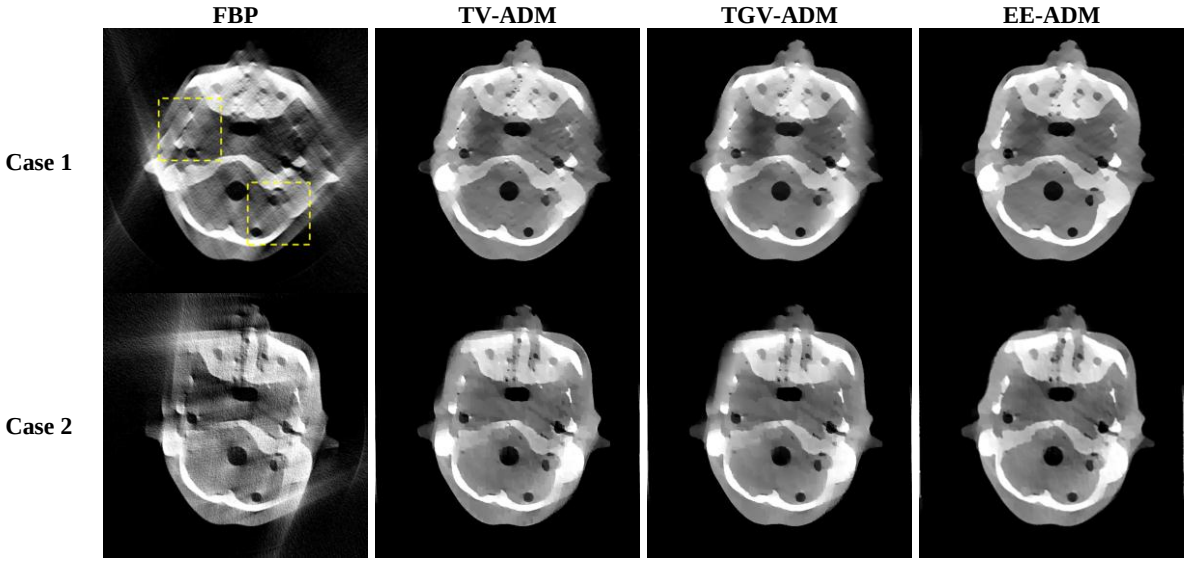

Fig. 11. Image reconstruction of the anthropomorphic head phantom. From left to right in each row, images reconstructed from FBP, TV-ADM, TGV-ADM, and EE-ADM methods are presented(C=100 HU/W=1500 HU).

0018-9499 (c) 2016 IEEE. Personal use is permitted, but republication/redistribution requires IEEE permission. See http://www.ieee.org/publications_standards/publications/rights/index.html for more information.

This article has been accepted for publication in a future issue of this journal, but has not been fully edited. Content may change prior to final publication. Citation information: DOI 10.1109/TNS.2017.2717864, IEEE Transactions on Nuclear Science

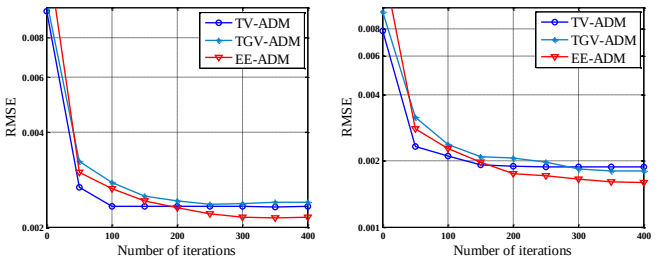

Fig. 14. Root mean square errors as a function of iteration steps for the three iterative methods in the anthropomorphic head phantom study.

TABLE III
EVALUATIONS OF THE RESULTS RECONSTRUCTED USING DIFFERENT ALGORITHMS IN THE ANTHROPOMORPHIC HEAD PHANTOM STUDY.

		TV-ADM	TGV-ADM	EE-ADM
Case 1	**RMSE**	2.332e-03	2.401e-03	2.149e-03
	PSNR	25.80 dB	25.55dB	26.51 dB
	UQI	0.9606	0.9595	0.9635
Case 2	**RMSE**	1.886e-03	1.809e-3	1.603e-03
	PSNR	26.41 dB	26.77dB	27.82 dB
	UQI	0.9678	0.9686	0.9711

C. Computation Time Comparison

The average computation time of TV-ADM and EE-ADM methods in the experimental studies are listed in Table IV. All experiments were performed under MATLAB 2012a running on a PC with an Intel i5-2400 3.10 GHz CPU. The projector and backprojector computations were accelerated using Gao's method [40] on a GTX 570 GPU. The table shows that the time consumption of EE-ADM method is a little longer than that of TGV-ADM method, and approximately 2.5 to 3 times longer than that of TV-ADM method. The additional time cost is spent on computing high-order variations.

TABLE IV
RUNNING TIME (IN CPU SECONDS) OF THE TV-ADM, TGV-ADM, AND EE-ADM METHODS FOR DIFFERENT EXPERIMENTAL STUDIES.

		TV-ADM	TGV-ADM	EE-ADM
Simulation	120 °scan	62.58	180.56	184.18
	90 °scan	57.47	174.82	178.15
Real data study	Case 1	30.84	82.28	84.81
	Case 2	30.58	82.25	84.04

VI. DISCUSSION AND CONCLUSION

Limited-angle CT image reconstruction is an open problem, and research on image prior-based regularization method is gaining interest in the field of X-ray CT. TV regularization method has been applied and has shown promise in image reconstruction from an incomplete projection dataset. However, in limited-angle scanning, the TV-based method presents blurred artifacts in the directions tangent to the missing projections in the reconstructed images. This paper presents a novel approach to the limited-angle image reconstruction problem that involves a curvature-based Euler's elastica regularization model. Compared with the TV-based and TGV-based methods, the new method yields images without the usual blurring and shows excellent edge preservation.

To yield a reasonable result, several parameters should be optimized and are likely to be involved in any iterative reconstruction design that can significantly influence results. Although we cannot provide the "best" selection strategy, the suggested metrics employing Euler's elastica regularization enables high-quality image recovery with limited-angle scanning coverage and provides a clinically useful potential for dental and breast radiographies.

One limitation of our method is the prolonged time caused by the computation of high-order derivatives. With the development of high-performance devices, this procedure could be accelerated using graphics-processing units.

The EE-ADM method presented in this work focuses only on CT image reconstruction based on limited-angle projections. However, the proposed method can also be used in other X-ray CT applications, including interior tomography and sparse-view reconstruction. Furthermore, it may mediate the limited-angle problems in geophysical exploration and radar imaging applications.

In conclusion, this paper presents an Euler's elastica model to recover edge information while avoiding the aliasing effect for limited-angle CT image reconstruction. The experimental results show that the Euler's elastica-based method can effectively suppress aliasing artifacts and improve image quality. The findings in this work enable a more accurate reconstruction for limited-angle tomography and suggest potential use for clinical diagnoses.

ACKNOWLEDGEMENT

This work is supported in part by the National Natural Science Foundation of China (No. 61372172, 61601518). The authors are also grateful to the anonymous reviewers for their constructive comments and suggestions.

REFERENCES

[1] M. Rantala, S. Vanska, S. Jarvenpaa, M. Kalke, M. Lassas, J. Moberg and S. Siltanen "Wavelet-based reconstruction for limited-angle X-ray tomography," *IEEE Trans. Med. Imaging* **25**(2), 210–217 (2006).

[2] Y. Zhang, H. P. Chan, B. Sahiner, W. Jun, M. B. Mitchell, M. H. Lubomir, G. Jun and Z. Chuan "A comparative study of limited-angle cone-beam reconstruction methods for breast tomosynthesis," *Med. Phys.* **33**(10), 3781–3795 (2006).

[3] M. K. Cho, H. Youn, S. Y. Jang and H. K. Kim "Cone-beam digital tomosynthesis for thin slab objects," *NDT & E International* **47**, 171–176 (2012).

[4] M. Nassi, W. Brody, B. Medoff and A. Macovski "Iterative reconstruction-reprojection: an algorithm for limited data cardiac-computed tomography," *IEEE Trans. Biomed. Eng*. **29**, 333–341 (1982).

[5] H. H. Barrett and K. J. Myers "Foundations of Image Science," (John Wiley & Sons, Hoboken, New Jersey, 2004).

[6] L. P. Jerry "Constrained sinogram restoration for limited-angle tomography," *Optical Engineering* **29**(5), 535–544 (1990).

[7] J. K. Choi, B. Dong and X. Zhang "Limited tomography reconstruction via tight frame and simultaneous sinogram extrapolation," arXiv preprint 1602.07049 (2016).

[8] H. Zhang, L. Li, L. Wang, Y. Sun, B. Yan, A. Cai and G. Hu "Computed tomography sinogram inpainting with compound prior modelling both sinogram and image sparsity," *IEEE Trans. Nucl. Sci*. **63**(5), 2567-2576, (2016).

0018-9499 (c) 2016 IEEE. Personal use is permitted, but republication/redistribution requires IEEE permission. See http://www.ieee.org/publications_standards/publications/rights/index.html for more information.

This article has been accepted for publication in a future issue of this journal, but has not been fully edited. Content may change prior to final publication. Citation information: DOI 10.1109/TNS.2017.2717864, IEEE Transactions on Nuclear Science

[9] G. H. Chen, J. Tang and S. Leng "Prior image constrained compressed sensing (PICCS): a method to accurately reconstruct dynamic CT images from highly undersampled projection data sets," *Med. Phys*. **35**, 660–663 (2008).

[10] T. Heußer, M. Brehm, L. Ritschl, S. Sawall and M. Kachelrieß "Prior-based artifact correction (PBAC) in computed tomography," *Med. Phys*. **41**(2), 021906 (2014).

[11] D. Wu, L. Li and L. Zhang "Feature constrained compressed sensing CT image reconstruction from incomplete data via robust principal component analysis of the database," *Phys. Med. Biol*. **58**, 4047–4070 (2013).

[12] E. Candes, J. Romberg and T. Tao "Robust uncertainty principles: exact signal reconstruction from highly incomplete frequency information ," *IEEE Trans. Inf. Theory* **52**, 489–509 (2006).

[13] E. Y. Sidky, C. Kao and X. C. Pan "Accurate image reconstruction from few-views and limited-angle data in divergent-beam CT, " *J. X-Ray Sci. Technol*. **14**, 119–139 (2006)

[14] E. Y. Sidky and X. C. Pan, "Image reconstruction in circular cone-beam computed tomography by constrained, total-variation minimization," *Phys. Med. Biol*. **53**, 4777–4807 (2008).

[15] H. Y. Yu and G. Wang, "Compressed sensing based interior tomography," *Phys. Med. Biol*. **54**, 2791–2805 (2009).

[16] L. Ritschl, F. Bergner, C. Fleischmann, and M. Kachelrieß, "Improved total variation-based CT image reconstruction applied to clinical data," *Phys. Med. Biol*. **56**, 1545–1561 (2011).

[17] H. Zhang, L. Wang, B. Yan, L. Li, X. Xi, and L. Lu. "Image reconstruction based on total-variation minimization and alternating direction method in linear scan computed tomography," *Chinese Phys B* **22**, 078701 (2013).

[18] J. Yang, H. Yu, M. Jiang, and G. Wang, "High-order total variation minimization for interior tomography," *Inverse Problems*, **26**, 035013 (2010).

[19] Y. Liu, Z. Liang, J. Ma, H. Lu, K. Wang, H. Zhang, and W. Moore, "Total variation-stokes strategy for sparse-view X-ray CT image reconstruction," *IEEE Trans. Med. Imaging* **33**, 749–763, (2014).

[20] S. Niu, Y. Gao, Z. Bian, J. Huang, W. Chen, G. Yu, Z. Liang, and J. Ma. Sparse-view X-ray CT reconstruction via total generalized variation regularization. *Phys Med Biol*. **59**, 2997-3017, (2014).

[21] J. Chen, L. Wang, B. Yan, H. Zhang, and G. Cheng. Efficient and robust 3D CT image reconstruction based on total generalized variation regularization using the alternating direction method. *J X-Ray Sci Technol*. **23**(6), 683-699, (2015).

[22] H. Zhang, L. Wang, B. Yan, L. Li, A. Cai, and G. Hu "Constrained total generalized p-variation minimization for few-view x-ray computed tomography image reconstruction," *PLoS One* **11**, e0149899 (2016).

[23] J. Frikel "Sparse regularization in limited angle tomography," *Applied and Computational Harmonic Analysis* **34**(1) 117–41 (2013).

[24] H. Zhang, L. Wang, L. Li, A. Cai, G. Hu, and B. Yan "Iterative metal artifact reduction for x-ray computed tomography using unmatched projector/backprojector pairs," *Med. Phys*. **43**, 3019–3033 (2016).

[25] H. Zhang, L. Li, B. Yan, L. Wang, A. Cai, and G. Hu "A two-step filtering-based iterative image reconstruction method for interior tomography,"*J. X-Ray Sci. Technol*. **24**(5), 733-747, (2016).

[26] E. T. Quinto "Tomographic reconstructions from incomplete data-numerical inversion of the exterior Radon transform," *Inverse Problems* **4**, 867–76 (1988).

[27] J. Frikel and E. T. "Quinto Characterization and reduction of artifacts in limited angle tomography," *Inverse Problems* **29**(12) 125007 (2013).

[28] Z. Chen, X. Jin, L. Li and G. Wang, "A limited-angle CT reconstruction method based on anisotropic TV minimization," *Phys. Med. Biol*. **58**, 2119–2141 (2013).

[29] T. F. Chan, S. H. Kang and J. Shen "Euler's elastica and curvature-based inpainting," *SIAM J. Appl. Math*. **63**(2), 564–594, (2002).

[30] X. C. Tai, J. Hahn and G. J. Chung "A fast algorithm for Euler's elastica model using Augmented lagrangian method," *SIAM J. Imaging Sci*. **4**(1), 313–344 (2011).

[31] Y. P. Duan, Y. Wang and J. Hahn "A Fast Augmented Lagrangian Method for Euler's Elastica Models," *Numer. Math. Theor. Meth. Appl*. **6**(1), 47–71 (2013).

[32] T. F. Chan and S. Jianhong "Nontexture inpainting by curvature-driven diffusions(CDD)," J. Visual Comm. Image Rep. **12**, 436–449, (2001).

[33] Y. Wang, J. Yang, W. Yin, and Y. Zhang. "A new alternating minimization algorithm for total variation image reconstruction," SIAM J. Imaging Sci. **1** 248–272 (2008).

[34] C. Li, W. Yin, H. Jiang, Y. Zhang, "An efficient augmented Lagrangian method with applications to total variation minimization," *Computational Optimization* and *Applications* **56**, 507–530 (2013).

[35] Y. Xiao, J. Yang, X. Yuan. "Alternating algorithms for total variation image reconstruction from random projections," *Inverse Problems and Imaging* **6**, 547–563 (2012).

[36] P. L. Lions and B. Mercier "Splitting algorithms for the sum of two nonlinear opertors," *SIAM J. Num. Anal*. **16**, 964–979 (1979).

[37] J. D. Pack, F. Noo and R. Clackdoyle "Cone-Beam Reconstruction Using the Backprojection of Locally Filtered Projections," *IEEE Trans. Med. Imaging* **24**(1), 70–85 (2005).

[38] International Commission on Radiation Units and Measurements, "Phantoms and computational models in therapy, diagnosis and protection," ICRU Report No.48 (ICRU Publications, Bethesda, MD, 1992).

[39] Z. Wang and A. C. Bovik, "A universal image quality index," *IEEE Signal Process. Lett*. **9**, 81–84 (2002).

[40] H. Gao, "Fast parallel algorithms for the X-ray transform and its adjoint," *Med. Phys*. **39**, 7110–7120 (2012).

0018-9499 (c) 2016 IEEE. Personal use is permitted, but republication/redistribution requires IEEE permission. See http://www.ieee.org/publications_standards/publications/rights/index.html for more information.